Article

Large metallicity variations in the Galactic interstellar medium

Annalisa De Cia[1 ✉], Edward B. Jenkins[2], Andrew J. Fox[3], Cédric Ledoux[4], Tanita Ramburuth-Hurt[1], Christina Konstantopoulou[1], Patrick Petitjean[5] & Jens-Kristian Krogager[1]

The interstellar medium (ISM) comprises gases at different temperatures and densities, including ionized, atomic and molecular species, and dust particles[1]. The neutral ISM is dominated by neutral hydrogen[2] and has ionization fractions of up to eight per cent[3]. The concentration of chemical elements heavier than helium (metallicity) spans orders of magnitudes in Galactic stars[4], because they formed at different times. However, the gas in the vicinity of the Sun is assumed to be well mixed and to have a solar metallicity in traditional chemical evolution models[5]. The ISM chemical abundances can be accurately measured with ultraviolet absorption-line spectroscopy. However, the effects of dust depletion[6–9]—which removes part of the metals from the observable gaseous phase and incorporates it into solid grains—have prevented, until recently, a deeper investigation of the ISM metallicity. Here we report the dust-corrected metallicity of the neutral ISM measured towards 25 stars in our Galaxy. We find large variations in metallicity over a factor of ten (with an average of 55 ± 7 per cent solar metallicity and a standard deviation of 0.28 dex), including many regions of low metallicity, down to about 17 per cent solar metallicity and possibly below. Pristine gas falling onto the Galactic disk in the form of high-velocity clouds can cause the observed chemical inhomogeneities on scales of tens of parsecs. Our results suggest that this low-metallicity accreting gas does not efficiently mix into the ISM, which may help us understand metallicity deviations in nearby coeval stars.

We analyse Hubble Space Telescope (HST) Space Telescope Imaging Spectrograph (STIS) near-ultraviolet spectra of 25 bright type-O and type-B stars in the Galaxy. When available, we include archival Very Large Telescope (VLT) Ultraviolet and Visual Echelle Spectrograph (UVES) high-resolution optical spectra of these targets. The selection of the 25 stars in our sample, as well as the data collection and handling, is described in Methods and the sample properties are listed in Extended Data Table 1. The locations of our targets on the Galactic plane are visualized in Fig. 1.

We identify and analyse the absorption lines from Mg I, Al II, Si II, Cr II, Fe II, Co II, Ni II, Zn II and Ti II. A selection of absorption lines in the spectra of our targets are shown in Extended Data Fig. 1. The column density measurements are explained in Methods and reported in Extended Data Table 2. We report 3σ significance levels for the quoted limits and 1σ for the quoted errors, unless otherwise stated.

We determine the neutral gas metallicity using two independent approaches and with different assumptions, which we call the 'relative' method and the 'F^*' method. Both methods aim to characterize the strength of dust depletion along Galactic lines of sight, and are described in Methods (equations (1)–(8)). We use both methods to cross-check our results. In brief, the F^* and relative methods use either the gas-phase abundances or the relative abundances to estimate by how much the observations are affected by dust depletion based on the empirical relations of ref. [8] or ref. [9], respectively. Each method uses

a specific parameter to estimate the overall amount of dust depletion in a system, either $[Zn/Fe]_{fit}$ or F^*, as explained in Methods.

The individual dust-corrected abundances derived with the relative method are shown in Fig. 2, for individual metals. Figure 3 shows the total metallicities towards the 25 lines of sight in our sample, which are listed in Extended Data Table 3 and derived with the relative and F^* methods from the fit to the data in Extended Data Figs. 2, 3, respectively. We measure total metallicities $[M/H]_{tot}$ ranging between −0.76 dex and +0.26 dex, where about two-thirds of our sample show subsolar metallicities. The average metallicity in our sample is −0.26 ± 0.06 dex (that is, 55 ± 7% solar) with a standard deviation of 0.28 dex. The most notable result is that the maximum variations between lines of sight are more than an order of magnitude, mostly subsolar. In Methods, we test this result for different assumptions. The result holds regardless of the assumptions. It is possible that the low metallicities that we measure represent a mix of two different gases, namely a nearly solar interstellar medium (ISM) component with high depletion levels with the injection of significant amounts of pristine gas with zero depletion and metallicities even lower than what we measure (Methods).

In addition, for some cases where we measure a low metallicity, the most volatile elements (for example, oxygen, carbon and krypton) show some disagreement with the mildly depleted elements (for example, zinc) and the more refractory elements (Extended Data Fig. 3). This is well explained by the presence of inhomogeneities in the ISM, where nearly solar-metallicity

[1]Department of Astronomy, University of Geneva, Versoix, Switzerland. [2]Princeton University Observatory, Princeton, NJ, USA. [3]AURA for ESA, Space Telescope Science Institute, Baltimore, MD, USA. [4]European Southern Observatory, Vitacura, Chile. [5]Institut d'Astrophysique de Paris, Sorbonne Universités & CNRS, Paris, France. ✉e-mail: annalisa.decia@unige.ch
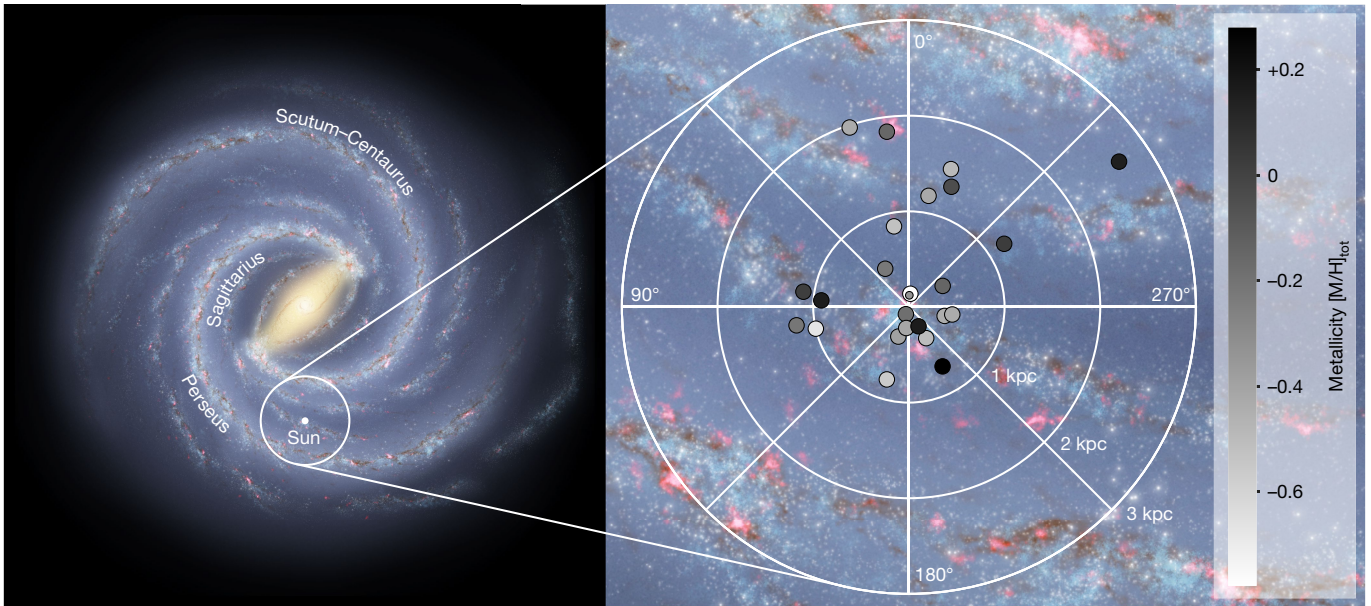
Fig. 1 | Location of our targets on the Galactic plane. Left, artistic impression of the Galaxy, face-on. Image courtesy of NASA/JPL-Caltech/R. Hurt (SSC/ Caltech). Right, the location of our targets is marked on the same illustration of the Galaxy, but zoomed-in on the star-forming spiral arms in the Solar neighbourhood. The metallicity of the neutral gas along these lines of sight (Extended Data Table 3) is highlighted with the greyscale. 1 kpc ≈ 3.09 × 10^{19} m.

gas is mixed with large amounts of pristine gas with zero depletion and low metallicity (for example, 10% solar or lower), as we discuss in Methods.

Although the metallicity of the Sun is about 0.2 dex higher than the expected metallicity of H II regions at a Galactic radius of 8.2 kpc[10], this is not enough to explain our results. Local chemical dilution or enrichment in the ISM could be caused by infalling gas or star formation, respectively, but the survival of such chemical inhomogeneities is not straightforward. A previous work[11] found that chemical enrichment due to supernovae can induce only small metallicity deviations of $Z \lesssim 10^{-1}$ between waves of star formation, after which Galactic rotation can mix the gas in a volume of about 0.1 kpc^3 within a timescale of 2.8×10^8 yr. However, dilution of disk metallicities to lower values could be caused by accretion of pristine gas, and these inhomogeneities could survive. Chemical evolution models indicate that low-metallicity gas infalling from the halo is necessary to fuel star formation and reproduce stellar abundance patterns[12,13]. Moreover, the large dispersion of the stellar age–metallicity relation[14] suggests a chemically inhomogeneous disk[4]. Episodic gas infall could produce pockets of low-metallicity gas and be responsible for the stellar age–metallicity scatter[15]. Analytical inhomogeneous chemical evolution models, which include non-instantaneous mixing of both infalling low-metallicity gas and enriched gas from star formation, showed that significant chemical inhomogeneities due to gas infall (or star formation) will arise if the mass of the new gas cloud is at least about 1/20 times the overall mass of the gas it is mixing into[16]. Simulations of supernova-driven metal enrichment and ISM mixing suggest that subkiloparsec-scale inhomogeneities in the ISM should survive at least on timescales of the order of 350 Myr[17]. Small subparsec-scale variations have been observed in the ISM[18,19].

Both observations and simulations indicate that gas infall onto the Galaxy halo is metal poor, with high-velocity cloud (HVC) metallicities observed in the range of 0.1–1 solar[20] and cosmological simulations predicting infalling gas to have metallicities as low as 0.01 solar[21]. More detailed zoom-in simulations show that infalling HVCs can fragment to scales below 30 pc and disperse on timescales of tens to hundreds of million years as they mix into the surrounding medium[22,23]. Metallicity inhomogeneities can therefore be smoothed out on these timescales. HVC clouds tend to have individual H I masses of a few 10^5 $M_\odot$ to 10^6 $M_\odot$ (in which $M_\odot$ is the mass of the Sun), for a total M(H I)$_{tot} \approx 10^7$ $M_\odot$ for our Galaxy[20]. Intermediate velocity clouds (IVCs), which tend to have higher

metallicities (solar) and smaller distances (<1–2 kpc) than HVCs[24,25], may also contribute to the dilution or enrichment of the ISM.

The rate of gas accretion on the Galaxy disk currently measured (0.1– 1.4 $M_\odot$ yr^{-1}) (refs. [26,27]) is a factor of about 100 larger than the minimum required to sustain the formation and survival of chemical inhomogeneities, as we estimate in Methods. Therefore, not only could pockets of low-metallicity/pristine gas exist but also they could in fact be very common. Here we found that two-thirds of our sample showed subsolar metallicity, but these measurements are integrated along the lines of sight, so that more pockets of lower-metallicity gas could exist. The minimum physical scale of the metallicity variations that we observe is of the order of tens of parsecs, and possibly down to a few parsecs (Methods). Our methodology opens up the possibility of comparing the metallicity of the neutral gas with the metallicity of stars and their H II regions, although this is not a straightforward comparison, as we discuss in Methods.

Finally, we find no positive correlations between the total metallicities and the reddening, or colour excess, between the blue and visual filters, $E(B-V)$, meaning that we do not observe higher reddening towards regions of higher metallicity. We do not find a significant correlation between R_V and metallicity, but we note that θ^1 Orionis C and ρ Ophiuchi A have high values of the total to selective extinction, R_V (Extended Data Table 1). The dilution of the ISM with lower-metallicity gas may have a role in explaining these effects. We do not observe any significant signs of a radial metallicity gradient in the gaseous disk, as shown in Extended Data Fig. 4. The observed metallicity gradients in the Galaxy have slopes of up to about −0.07 dex kpc^{-1}, from measurements of stars[28] and H II regions[10], but they are probed over several kiloparsecs. Our measurements cover a much narrower range (3 kpc) and with smaller statistics. A larger sample is needed for further conclusions on a potential gradient. We also do not observe any trend of metallicity with Galactic height, as shown in Extended Data Fig. 4. Thus, it is unlikely that the accreting gas is evenly distributed above the disk, but it is consistent with being clumpy, as in HVCs or tidal streams. However, our targets mostly lie within the young thin disk, probing small height scales. The global effects in chemical enrichment of inflowing and outflowing gas above the galaxy disks can be more evident at circumgalactic scales[29].

We conclude that we have measured large local variations of metallicity in the neutral ISM in our Galaxy probably due to accretion of low-metallicity gas. Thus, we recommend changing the common assumptions that the gas in galaxies is well mixed and the gas in the Galaxy has
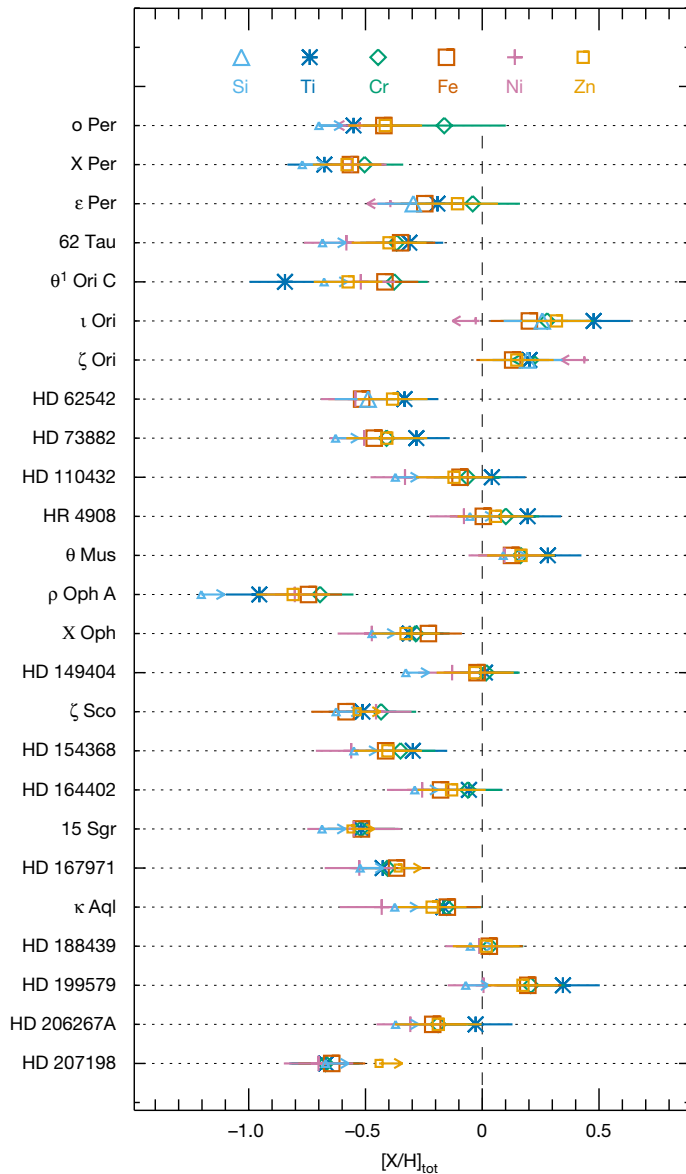
Fig. 2 | Dust-corrected abundances in the neutral ISM. Dust-corrected abundances of Si (light-blue triangles), Ti (blue stars), Cr (green diamonds), Fe (vermilion squares), Ni (pink crosses) and Zn (yellow squares) using the relative method. Stars are labelled in order of HD number (Extended Data Table 1). The error bars show the 1σ uncertainties.

Fig. 3 | Metallicities in the neutral ISM. Dust-corrected metallicities are marked with circles: the filled blue circles are derived with the relative method and the open green circles with the F^* method. The open yellow triangles show the observed [Zn/H], and thus represent a lower limit to the true metallicity. Stars are ordered with increasing metallicity. In our sample, 15 out of 25 lines of sight are more than 3σ away from solar metallicity (horizontal dashed line). The error bars show the 1σ uncertainties.

1. Draine, B. T. *Physics of the Interstellar and Intergalactic Medium* (Princeton Univ. Press, 2011).
2. Viegas, S. M. Abundances at high redshift: ionization correction factors. *Mon. Not. R. Astron. Soc.* **276**, 268–272 (1995).
3. Jenkins, E. B. The fractional ionization of the warm neutral interstellar medium. *Astrophys. J.* **764**, 25 (2013).
4. McWilliam, A. Abundance ratios and galactic chemical evolution. *Annu. Rev. Astron. Astrophys.* **35**, 503-556 (1997).
5. Matteucci, F. *Chemical Evolution of Galaxies* (Astronomy and Astrophysics Library, Springer, 2012).
6. Field, G. B. Interstellar abundances: gas and dust. *Astrophys. J.* **187**, 453–459 (1974).
7. Savage, B. D. & Sembach, K. R. Interstellar abundances from absorption-line observations with the Hubble Space Telescope. *Annu. Rev. Astron. Astrophys.* **34**, 279–330 (1996).
8. Jenkins, E. B. A unified representation of gas-phase element depletions in the interstellar medium. *Astrophys. J.* **700**, 1299–1348 (2009).
9. De Cia, A. et al. Dust-depletion sequences in damped Lyman-α absorbers. A unified picture from low-metallicity systems to the Galaxy. *Astron. Astrophys.* **596**, A97 (2016).
10. Arellano-Córdova, K. Z., Esteban, C., Garca-Rojas, J. & Méndez-Delgado, J. E. The Galactic radial abundance gradients of C, N, O, Ne, S, Cl, and Ar from deep spectra of H II regions. *Mon. Not. R. Astron. Soc.* **496**, 1051–1076 (2020).
11. Edmunds, M. G. Is the Galactic Disk well mixed? *Astrophys. Space Sci.* **32**, 483–491 (1975).
12. Tosi, M. The effect of metal-rich infall on galactic chemical evolution. *Astron. Astrophys.* **197**, 47–51 (1988).
13. Chiappini, C., Matteucci, F. & Gratton, R. The chemical evolution of the Galaxy: the two-infall model. *Astrophys. J.* **477**, 765–780 (1997).
14. Edvardsson, B. et al. The chemical evolution of the Galactic disk. I. Analysis and results. *Astron. Astrophys.* **275**, 101–152 (1993).
15. Pilyugin, L. S. & Edmunds, M. G. Chemical evolution of the Milky Way Galaxy. II. On the origin of scatter in the age–metallicity relation. *Astron. Astrophys.* **313**, 792–802 (1996).
16. White, S. D. M. & Audouze, J. Stochastic effects in the chemical evolution of galaxies. *Mon. Not. R. Astron. Soc.* **203**, 603–618 (1983).
17. de Avillez, M. A. & Mac Low, M. M. Mixing timescales in a supernova-driven interstellar medium. *Astrophys. J.* **581**, 1047–1060 (2002).
18. Andrews, S. M., Meyer, D. M. & Lauroesch, J. T. Small-scale interstellar Na I structure toward M92. *Astrophys. J. Lett.* **552**, L73–L76 (2001).
19. Nasoudi-Shoar, S., Richter, P., de Boer, K. S. & Wakker, B. P. Interstellar absorptions towards the LMC: small-scale density variations in Milky Way disc gas. *Astron. Astrophys.* **520**, A26 (2010).
20. Fox, A. J. & Davé, R. *Gas Accretion onto Galaxies* (Astrophysics and Space Science Library 430, Springer, 2017).
21. Wright, R. J., Lagos, C. P., Power, C. & Correa, C. A. Revealing the physical properties of gas accreting to haloes in the EAGLE simulations. *Mon. Not. R. Astron. Soc.* **504**, 5702–5725 (2021).
22. Gritton, J. A., Shelton, R. L. & Kwak, K. Mixing between high velocity clouds and the Galactic halo. *Astrophys. J.* **795**, 99 (2014).
23. Heitsch, F. & Putman, M. E. The fate of high-velocity clouds: warm or cold cosmic rain? *Astrophys. J.* **698**, 1485–1496 (2009).
24. Putman, M. E., Peek, J. E. G. & Joung, M. R. Gaseous galaxy halos. *Annu. Rev. Astron. Astrophys.* **50**, 491–529 (2012).
25. Richter, P. *Gas Accretion onto the Milky Way* (Astrophysics and Space Science Library 430, Springer, 2017).
26. Lehner, N. & Howk, J. C. A reservoir of ionized gas in the Galactic halo to sustain star formation in the Milky Way. *Science* **334**, 955–958 (2011).
27. Fox, A. J. et al. The mass inflow and outflow rates of the Milky Way. *Astrophys. J.* **884**, 53 (2019).
28. Cheng, J. Y. et al. Metallicity gradients in the Milky Way disk as observed by the SEGUE survey. *Astrophys. J.* **746**, 149 (2012).
29. Wendt, M., Bouché, N. F., Zabl, J., Schroetter, I. & Muzahid, S. MUSE gas flow and wind V. The dust/metallicity-anisotropy of the circum-galactic medium. *Mon. Not. R. Astron. Soc.* **502**, 3733–3745 (2021).

solar metallicity in the solar vicinity, which are widely used both in observational and theoretical works, and in particular for the study of the chemical evolution of the Galaxy. Our findings that the gas is inhomogeneously distributed (not only chemically) indicate that the gas mixing is more inefficient than previously thought. One of the potential causes could be the fact that the different phases involved in the mixing have widely different kinematics and different physical conditions. In addition, substantial sustained gas inflow may contribute to the clumpiness and turbulent nature of the disk in addition to gravitational instabilities.

Online content

Any methods, additional references, Nature Research reporting summaries, source data, extended data, supplementary information, acknowledgements, peer review information; details of author contributions and competing interests; and statements of data and code availability are available at https://doi.org/10.1038/s41586-021-03780-0.
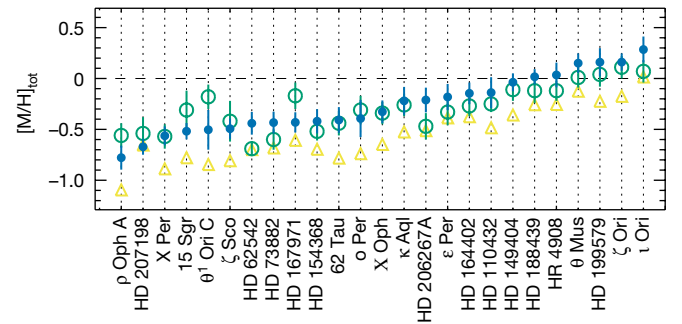
Methods

Sample selection and data collection

We select 25 stars and observe them as part of the cycle 25 HST programme ID 15335 (principal investigator A.D.C.). The sample was selected to include hot stars (spectral type O or type B) that have line-of-sight measurements of H I, H$_2$ and Ti II in the literature[30–32], high-enough rotational velocities ($\gtrsim$50 km s^{-1}) to allow us to disentangle between stellar and ISM features in the spectra, and fairly diverse values of dust reddening and Galactic longitude. The distances r are taken from the Gaia Data Release 2 (DR2) archive[33,34]. The values of H I and H$_2$ are taken from ref. [31] and ref. [32], respectively, as also collected by ref. [30] for most of our targets, and assuming their average uncertainties of 0.1 dex. For HD 62542, we adopt the column densities of atomic and molecular hydrogen from ref. [35]. The main characteristics of the 25 selected stars are reported in Extended Data Table 1.

The reddening $E(B - V)$ of the stars in our sample is taken from ref. [31] and spreads between 0.07 mag and 1.08 mag. The values of the optical total-to-selective extinction ratio, $R_V = A_V / E(B - V)$, in which A_V is the dust extinction in the visual band, are taken from the maps of ref. [36] and show variations between 2.6 and 5.7. The positions of the stars are distributed in Galactic longitude, their distances are within 2.7 kpc from the Sun and they lie within 0.3 kpc from the disk plane. All lines of sight have total hydrogen column densities ($N(H) = N(H I) + 2 \times N(H_2)$) that are high enough to shield the gas against photoionization[2]. We further discuss potential ionization effects below.

All stars are observed with the same HST/STIS Near-UV echelle setting E230M (at a central wavelength setting of 1,978 Å), which covers the absorption lines between about 1,605 Å and about 2,832 Å with a resolving power $R = \Delta\lambda/\lambda \approx 30,000$ at wavelength λ.

We further collected all the available reduced VLT/UVES spectra in the European Southern Observatory (ESO) Science Archive covering Ti II λ3230, 3242, 3384 lines for our sample, which are available for 16 of our targets and have $R \approx 71,050$. We stack the spectra for each star to maximize the signal-to-noise ratio, and measure the Ti II column densities in the same way as for the other metals, which are reported in Extended Data Table 2. In the event that no data that cover Ti II are available, we adopt the Ti II column densities of ref. [30].

For the star HD 62542, we include the column densities that were recently measured by ref. [35] from HST data at a higher spectral resolution. Given the better quality of these data, we adopt their column densities for both of their velocity components summed together for our analysis.

Analysis of the absorption features and column-density determination

We identify and analyse the following absorption lines: Mg I λ1827, 2026; Al II λ1670; Si II λ1808; Ti II λ3230, 3242, 3384; Cr II λ2056, 2062, 2066; Fe II λ2344, 2260, 2249; Co II λ2012, 1941 (although we did not use the column densities of Co II in our analysis); Ni II λ1741, 1709, 1751; Zn II λ2026, 2062. The line profiles of the Zn II λ2026, Cr II λ2056 and Fe II λ2260 transitions are shown in Extended Data Fig. 1. The velocity extremes over which we performed absorption line measurements appear to be well defined by the maximum extent of the very strong Fe II λ2344 transition. We used the most recent oscillator strengths (f values), listed in Extended Data Table 4. We determined the column densities by integrating the apparent optical depths (AODs)[37] over all velocities between these extremes, regardless of the appearance of the line in question. This procedure guaranteed that we did not overlook weak parts of an absorption buried in the noise, and also prevented us from defining a continuum level partly within the extent of such absorption. We defined continuum levels from best-fitting Legendre polynomials to fluxes on either side of the absorption profiles. Some lines appeared to be saturated or nearly so; in such cases, the AOD method can underestimate the true column density. When the lowest part of a feature seemed close to the zero intensity level but still had

a pointed appearance, we considered saturation to be taking place and declared the measurement as a lower limit. The Fe II λ2344 line was often heavily saturated, but weaker Fe II lines (λ2260, 2249) were well constrained. In most circumstances, the two lines of Zn II did not appear to be appreciably saturated, but the fact that the stronger λ2026 line consistently gave a column density that was lower than the weaker λ2062 line indicated that some unresolved saturation was still creating column-density outcomes that were below the true ones. To overcome this problem, we invoked the scheme proposed by ref. [38] that applies a correction to arrive at a more accurate column density. The contribution of nearby Mg I λ2026 and Cr II λ2062 features were taken into account for the calculation of the Zn II column density. We estimated errors for the column densities from the effects of three different sources: (1) noise in the absorption profile, (2) errors in defining the continuum level and (3) uncertainties in the transition f values, all of which were combined in quadrature. Continuum placement errors can have a large influence in the uncertainties of weak lines. We evaluated the expected deviations produced by such errors by remeasuring the AODs at the lower and upper bounds for the continua, which were derived from the expected formal uncertainties in the polynomial coefficients of the fits as described by ref. [39]. We multiplied these coefficient uncertainties by two to make approximate allowances for additional deviations that might arise from some freedom in assigning the most appropriate order for the polynomial. We considered a measurement to be marginal if the equivalent width outcome was less than the 2σ level of uncertainty from noise and continuum placement. For weak lines below this uncertainty threshold, we specified an upper limit for the column density. Details of how we calculated these 1σ upper limits are given in appendix D of ref. [40]. If the strongest transition yielded an upper limit or a very marginal detection, no attempt was made to measure considerably weaker ones except when a weaker line was in a much better part of the spectrum (higher signal-to-noise ratio or a more easily defined continuum).

We use a linear unit for the column densities N in terms of ions per square centimetre. We refer to relative abundances of elements X and Y as $[X/Y] \equiv \log \frac{N(X)}{N(Y)} - \log \frac{N(X)_\odot}{N(Y)_\odot}$, where reference solar abundances are listed in ref. [9].

Potential saturation effects and comparison with the Voigt-profile fit method

Saturation effects do not have an important role for the results presented in this Article. If present, any potential saturation effect must be small, and in particular much smaller compared with the strong effects of dust depletion. This can be immediately appreciated by the small deviations from the linear fits in Extended Data Figs. 2, 3. In addition, if saturation of Zn II was an issue, we should see more deviations in the dust-corrected abundances of Zn at solar metallicity (Fig. 2), which are not observed.

Nevertheless, we tested the robustness of the column-density determinations with the AOD method with an independent method, the Voigt-profile fit, which decomposes and models the line profiles in their individual velocity components and fits all transitions simultaneously. The Voigt-profile fit can use narrow broadening-parameters (b values) to account for saturation. These tests are aimed at further assessing the potential saturation of Zn II absorption lines. The saturation for other ions considered here is less probable because of the availability of weaker absorption lines to measure. Using the VoigtFit software[41], we model lines of Zn II and Cr II towards the eight targets that have the strongest Zn II absorption and show potential for saturation (Extended Data Fig. 4) and with a column density of Zn II constrained with the AOD method (Extended Data Table 2), namely: θ^1 Ori C, HD 73882, HR 4908, θ Muscae, HD 149404, HD 154368, HD 199579 and HD 206267. This includes the most troublesome target, θ^1 Ori C, which we discuss below.

For the seven out of the eight lines of sight tested, with the exception of θ^1 Ori C, the column densities of Cr II measured with the AOD and

Article

Voigt-profile fit are in excellent agreement (mostly within 0.03 dex and consistent within the errors) and the column densities of Zn II measured with the Voigt-profile fit differ by +0.03, +0.22, −0.1, −0.1, −0.02, −0.08 and +0.06 dex with respect to the AOD results, corresponding to 0.2, 1.8, 2.6, 1.0, 0.3, 1.0 and 0.5σ (Z-test) for HD 73882, HR 4908, θ Mus, HD 149404, HD 154368, HD 199579 and HD 206267, respectively. These are mostly typical values for the comparison between AOD and the Voigt-profile fit. The larger discrepancies are measured for HR 4908 and θ Mus, towards which we estimated near-solar metallicity (Extended Data Table 3).

A different picture arose for θ^1 Ori C, for which we measured significant differences of +0.33 dex and +0.45 dex with respect to the AOD results, corresponding to 7.4σ and 3.6σ (Z-test), for Zn II and Cr II, respectively. However, the Voigt-profile fit of the HST/STIS data was not well constrained for this system. This is probably caused by the extreme complexity of this line of sight[42], which cannot adequately be decomposed with the sampling of 5 km s^{-1} per pixel of the HST/STIS data. However, with a Voigt-profile fit to the VLT/UVES data, we obtained consistent measurements (within 1σ) with the AOD Ti II results and the results of ref. [42] for Ca II. The complexity of this line of sight may also explain the discrepancies among the different metals that we observe in Extended Data Figs. 2, 3. In the latter, the Zn II column is significantly below the linear fit, so that an increase in Zn II column would not affect heavily the result. These discrepancies are the likely cause of the difference in metallicity that we measured towards this line of sight with the relative and F^* methods (Extended Data Table 3).

Overall, our results hold regardless of whether the Voigt-profile fit or AOD method is used for estimating the column densities.

Ionization effects on column-density measurements

Owing to the background radiation field in the ISM, the atoms in the gas phase are found in various ionization states (for example, C II/C IV and Al II/Al III). In the neutral medium, the singly ionized metals are the dominant species due to their ionization potentials relative to that of H I. To obtain metallicities, we assume that other ionization states are negligible such that $N(X)/N(H) = \sum_i N(X_i)/(N(H\ I) + N(H\ II))$, where the summation is over all ionization states (i) of a given metal, X. However, if the total integrated absorption line arises from many unresolved components with varying physical properties, it is possible that this assumption does not hold for individual components. Such ionization corrections could therefore affect our conclusions about a difference in metal enrichment being the driver of the variations in the depletion sequences.

In all but three lines of sight, we detect absorption from neutral carbon (with an ionization potential lower than that of H I), which indicates that the gas phase must be highly shielded by H I. For the three cases where no clear C I absorption is seen (ε Persei, ι Ori and ζ Ori A), the non-detections are consistent with the overall low optical depth of other lines. The C I line profiles resemble those of the singly ionized metals indicating that they arise from the same gas phase. These facts provide strong evidence that the gas is effectively shielded; hence, ionization corrections can be neglected.

If ionization effects were the culprit of the observed deviations in the relative abundances, and not differential dust depletion, then the oxygen abundance should not follow those of the other volatile elements given the tight relationship between H I and O I (due to charge exchange reactions). However, in the cases where we can constrain the oxygen abundance, we see that it does indeed show the same behaviour as the heavier volatile elements. This further bolsters our conclusion that ionization effects are negligible.

The relative and F^* methods to measure the ISM metallicity

To measure the ISM metallicity, it is essential to quantify the amount of metals that are missing from the observable gas phase but instead are incorporated into dust grains, which is the phenomenon of dust depletion[6–9,43–45]. The dust-corrected (total of gas and dust) abundances can be defined as

$$[X/H]_{tot} = [X/H] - \delta_X , \tag{1}$$

where [X/H] is the observed abundance of metal X and δ_X is its depletion in dust (which is a negative term in this classical notation). Here no other effects such as nucleosynthesis or ionization are taken into account. The depletion δ_X is linearly proportional to the overall strength of depletion[8,9,45]. The overall strength of depletion can be represented in different ways, for example, from the observed relative abundances, as in the relative method, or with a specific parameter F^*, as in the F^* method.

The relative method was first introduced by ref. [9], which compared Galactic and extragalactic observations. To estimate the overall strength of depletion, this method uses any relative abundance [X/Y] where X and Y follow each other in nucleosynthesis, but have very different refractory properties. A dust tracer can be [Zn/Fe], or other relative abundances such as [Si/Ti] or [O/Si]. Previous work[46] discusses in more detail why [Zn/Fe] is a reliable dust tracer in the metallicities ranges considered here. The depletion of element X, δ_X, is obtained from the observed correlation between [X/Y] (with Y being non-refractory, such as S or P; here we use Zn) and the dust tracer [Zn/Fe] (or any other dust tracer). The dependency of [X/Zn] on the depletion of Zn can be removed by assuming a certain slope for the expected depletion of Zn with the dust tracer, $B_{\delta Zn}$. Then δ_X can be derived as follows:

$$\delta_X = A2_X + B2_X \times [Zn/Fe] , \tag{2}$$

where $A2_X$ and $B2_X$ are empirically determined coefficients and are reported in Extended Data Table 5. The simplest version of the relative method uses directly the observed [Zn/Fe] to estimate the dust depletion of the different metals. However, the information on all metals can be used simultaneously to determine the overall strength of the dust depletion with the parameter $[Zn/Fe]_{fit}$, which is equivalent to [Zn/Fe] but is derived from the information of all metals. Merging equations (1), (2), and using the basic definition of [X/H], it is possible to find the dust-corrected metallicity and overall strength of depletion from the observed metal column densities, through a fit of the linear relation

$$y = a + bx , \tag{3}$$

where

$$a = [M/H]_{tot} , \tag{4}$$

$$b = [Zn/Fe]_{fit} , \tag{5}$$

$$x = B2_X , \tag{6}$$

$$y = \log N(X) - \log N(H) - \log (X/H)_\odot - A2_X \tag{7}$$

and considering the uncertainties on both x and y. x and y represent the depletion data for different metals, and we fit a linear relation to this data to find the parameters a and b, which are unique to each system. In this way, the y intercept (at x = 0) of the fitted relation gives the total metallicity, $[M/H]_{tot}$, and its slope gives the overall strength of depletion, $[Zn/Fe]_{fit}$. Extended Data Fig. 5 illustrates this procedure for our sample. The fitted and observed [Zn/Fe] often agree well (Extended Data Table 3).

Changes in relative abundances could in principle be caused by nucleosynthesis processes or other reasons. In particular, deviations from the curves of Extended Data Figs. 2, 3 could in principle be caused by nucleosynthesis. However, the relative abundance patterns that we

observe here mostly follow the refractory properties of the metals, rather than their nucleosynthesis origin, and are therefore caused purely by dust depletion. We do not expect the infalling gas to have been enriched in specific metals or show or have any peculiar abundances due to different nucleosynthetic history. Alternatively, one could have the opportunity to investigate such peculiar abundances by studying eventual deviations from the depletion patterns.

The choice of $B1_{\delta Zn}$ is the main assumption of the relative method used here to find dust-currected metallicities. First, it is reasonable to assume that δ_{Zn} correlates linearly with [Zn/Fe] or other dust tracers, because this is observed for all other metals[8,9]. Moreover, we know that at [Zn/Fe] = 0, there is no dust depletion of non-carbonaeous species and we can safely assume no depletion of Zn, that is, $\delta_{Zn} = 0$ at [Zn/Fe] = 0. Thus, the main free parameter in the assumption of the Zn depletion is the slope of the relation of δ_{Zn} with [Zn/Fe], $B1_{\delta Zn}$. Here we assume $B1_{\delta Zn} = -0.27 \pm 0.03$ derived by ref. [9]. We conservatively test our results for different slope assumptions, as described below, to ensure that our ultimate results are not affected. Notably, the $A2_X$ and $B2_X$ coefficients for Ti are not well constrained so far, and this is a weakness of the relative method. However, this does not affect the overall results of this Article, which can mostly be derived already from the basic version of the relative method, using only the observed [Zn/Fe] and regardless of Ti, with the exception of those systems where $N(Zn)$ is not constrained.

The F^* method, first developed by ref. [8], characterizes the dust depletion in Galactic clouds, by correlating all the observed abundances and minimizing the residuals with respect to a common factor, F^*. This factor represents the overall strength of dust depletion in individual lines of sight. This method assumes that the underlying metallicity is solar. In an analogous way to that described above, the metallicities are found by fitting the linear relation

$$y = \log N(X) - \log N(H) - \log (X/H)_\odot - B_X + A_X \times z_X, \qquad (8)$$

where the A_X, B_X and z_X coefficients are determined and listed in ref. [8]. The definition of y differs by $-\log N(H)$ with respect to ref. [8]. The fit of this $y = a + bx$ relation, where $x = A_X$ yields a y intercept at $x = 0$ equal to [M/H]$_{tot}$, and $b = F^*$.

Extended Data Figure 2, 3 show how the relative and F^* methods fit the overall strength of dust depletion ([Zn/Fe]$_{fit}$ or F^*) and total (dust corrected) metallicity [M/H]$_{tot}$ to the the observed column densities. There is an overall good agreement between the total metallicity resulting from the relative method and the F^* method (Fig. 3), with a few notable exceptions, that is, for θ^1 Ori C and HD 62542. These are cases of peculiar abundances in particular of Ti, and possibly Zn, that make the depletion patterns vary considerably from the norm, as visible in Extended Data Figs. 2, 3. HD 62542 is a case with strong ISM inhomogeneities along the line of sight, with one cloud having a much stronger depletion than the others[35], and maybe also different metallicities.

The main assumption in the original establishment of the F^* method is that the metallicity of the gas is solar, and this assumption was used to compute the A_X, B_X and z_X coefficients[8]. That is, the individual observed [X/H] used to determine A_X and B_X are treated as pure signs of dust depletion, not including any potential variation in metallicity. However, the A_X and B_X coefficient determination could be altered, in case of significant deviations from the solar metallicity, such as potential several low-metallicity clouds.

Both the relative and F^* methods are sensitive to the effect of potential ISM dishomogeneities along the line of sight, which we discuss below.

Testing the assumptions of the relative method
We test our results using different assumptions on the slope of the Zn depletion sequence $B_{\delta Zn}$, which is the main assumption of the relative method, for the basic version of the method, that is, relying on the observed [Zn/Fe] only to characterize the δ_X. In addition to the optimal slope for the depletion of Zn ($B_{\delta Zn} = -0.27$; ref. [9]), we test for slopes that are two times steeper, two times shallower and from the relations of ref. [8]. (1) Assuming a steeper slope ($B_{\delta Zn} \equiv -0.54$), the resulting dust-corrected metallicities are 0.3–0.4 dex higher than using the optimal slope. However, such steep depletion of Zn is quite extreme and very difficult to reconcile with the independent work on dust depletion of ref. [8] (see figure 5 in ref. [9]). We consider this only as an extreme option of our parameter space to explore the potential impact on our results. (2) Assuming a shallower slope ($B_{\delta Zn} \equiv -0.135$), the resulting dust-corrected metallicities are 0.15–0.2 dex lower than using the 'reference' slope $B_{\delta Zn}$. This assumption is a potentially plausible option. (3) Finally, we assume that the depletion of Zn has the distribution of ref. [8] and use the (assumed) linear correlation between F^* and [Zn/Fe][9], and thus assuming $A_{\delta Zn} = 0.785$ and $B_{\delta Zn} = -0.904$. The extrapolation of this correlation to negative F^* is not necessarily reliable. Overall, the slopes for the metal depletion of ref. [8] are steeper than in ref. [9]. The metallicities derived with this last assumption are overall similar to those using the optimal slope, with a few local variations towards higher metallicities, in one case up to 0.3 dex. One common feature of our results, regardless of the assumption on the Zn depletion (and even including the less likely assumptions) is a wide spread in metallicities of about 1 dex.

The influence of ISM inhomogeneities along the line of sight
One important concern is the presence of line-of-sight inhomogeneities, and in particular whether our methods of estimating the metallicities could be affected by the ISM being composed of individual clouds with very different depletion strengths and/or metallicities. One example of such inhomogeneities is star HD 62542, for which individual components with very different depletion properties have been observed with higher-resolution spectroscopy (figure 6 in ref. [35]). Most Ti II line profiles in the stacked UVES spectra in our sample show asymmetry or complexity in the velocity structure, hinting at potentially separate clouds or inhomogeneous ISM along the line of sight.

We test the application of our methods for the case of two individual ISM components with different combinations of amount of gas, depletion and metallicity. If the two individual components have the same metallicity, the metallicity determination that we would estimate from the combined total column densities (over the whole line profiles) would be accurate, provided we use the y variables as defined in equations (7), (8). However, if the two ISM components have not only very different depletion strengths but also very different metallicities, then our estimates of the metallicity using the combined total column densities is in between the metallicities of the two clouds, and mostly closer to the components that carries most gas. For example, if one component has $F^* = 1$, solar metallicity and carries 10% of the gas, while the second component has $F^* = 0$, 10% solar metallicity and carries 90% of the gas, the relative method finds a global metallicity of 18% solar.

The injection of pristine gas (metal-poor gas with zero depletion levels) in the ISM can bring strong deviations from a straight-line fit in the x versus y plots, which affects the metallicity determination. If the line-of-sight ISM is composed of two clouds carrying the same amount of gas, the first one with [Zn/Fe] = 1.6 and solar metallicity, and the second one with [Zn/Fe] = 0 and 10% solar metallicity, then the relation between the total x and y (from column densities measured over the whole line profiles) in the relative method strongly departs from a straight line, with a curvature where the more volatile elements have higher than expected y values.

In fact, we observe sometimes large discrepancies between the observed abundances of the highly volatile elements (for example, O, Kr, C and N) taken from the literature[8,47] (Extended Data Table 6) on the one hand and the observed abundances of the mildly volatile elements (for example, Zn) and the refractory elements on the other hand, which is hard to interpret with the classic knowledge of dust depletion. This effect is highlighted in Extended Data Fig. 3, and is observed for several lines of sight in our sample, but only among those for which we find low metallicities (namely, o Per, X Per, 62 Tauri,

HD 62542, ρ Oph A, χ Oph, HD 154368, 15 Sagittarii and HD 207198). Classically, this effect was attributed to very high values of $F*$ (1–1.6), but with the difficulty of reconciling the overall depletion patterns. These abundance patterns can also not be attributed to nucleosynthesis effects. In principle, there could be intrinsic differences between O and N because of their different nucleosynthetic origin (primary α-capture process or secondary processes). However, only in one case we report measurements of N only among the volatile elements (HD 110432, Extended Data Fig. 3), and otherwise the measurements of N agree with all the other volatile elements.

Here we suggest that the large differences between the observed abundances of the most volatile elements with respect to Zn and the refractory elements are the effect of a substantial injection of pristine gas (with low metallicity, for example, 10% solar and no dust depletion) to the main ISM component with more typical (solar) metallicity and depletion levels. In our calculations, we assume that the pristine gas with no depletion has 10% solar metallicity, but it could have even lower metallicities. Dust depletion is often observed at high redshift in systems with 10% solar metallicity[48].

The line of sight towards HD 62542 is a good, and perhaps extreme, example of a case where two (or more) ISM components have very different depletion properties (one with extremely high $F* = 1.5$ and the rest with $F* = 0.3$, confirmed with higher-resolution spectroscopy). But even after taking this into account, the observed abundances do not fit the depletion patterns well[35]. In our analysis, we found subsolar values of metallicities, although we only considered the total columns measured over the whole line profile. Thus, we speculate that additional ISM mixing effects, and in particular with gas at subsolar metallicities, may in fact help reconcile the observations.

Overall, in the case of an inhomogeneous ISM with contributions of gas at different metallicities, our total metallicity estimates probably represent a value in between the lowest and highest metallicities, depending on how much gas the clouds bear. Our results witness significant amounts of low metallicity gas. Some of these could potentially represent a mix between nearly solar metallicity and pristine gas, with even lower metallicities than our integrated estimates.

Estimates of the gas accretion rate

We roughly estimate the minimum accretion rate required for clouds of gas not to mix efficiently, which would allow chemical inhomogeneities to survive. We assume that a volume $V_{mix} \approx 0.1$ kpc³ completely mixes within a timescale of $\tau_{mix} = 2.8 \times 10^8$ yr due to Galactic rotation[11], and calculate the mass of this mixing volume by assuming a number density. For this, we compute the average number densities along the lines of sight in our sample, $n_H = N(H)/r$ using only the accurate distance measurements from Gaia DR2, and adopt their mean value $<n_H> = 2.3$ cm⁻³. This is a typical value for the warm neutral medium[1]. The mass of the mixing region is then $M_{mix} \approx 6.2 \times 10^6 M_\odot$. Given the minimum mass fraction for chemical inhomogeneities to survive (1/20) (ref. [16]), the minimum accreting mass that can lead to a long-lived chemical inhomogeneity is $m_{min,acc} \approx 3.1 \times 10^5 M_\odot$. This is comparable to the mass of a small HVC cloud[20]. Overall, the minimum accretion rate that allows chemical inhomogeneities to survive Galactic rotation is $R_{min,acc} = m_{min,acc}/\tau_{mix} \approx 0.001 M_\odot$ yr⁻¹. This is much smaller than the typical accretion rate in the Galaxy, which is estimated to be around 0.1–1.4 $M_\odot$ yr⁻¹ from UV observations of HVCs[26,27], not including the Magellanic Stream. That is, the rate of gas accretion that is currently measured is more than enough (by a factor of about 100) to account for the existence and survival of chemical inhomogeneities. This is true even if we assume a mean number density of ten times higher, typical of the cold neutral medium, in which case $R_{min,acc}$ would be ten times higher.

Estimates of the physical scale of the metallicity variations

The physical scale of the metallicity variations cannot be easily estimated, because of the sparsity of our targets, and the fact that we measure the integrated metallicity along their lines of sight. The smallest scales can perhaps be probed in the Orion region, in which we observed metallicity variations towards three targets. The angular separation between θ¹ Ori C, a likely low-metallicity line of sight, and ι Ori and ζ Ori A is about 30.7′ and about 3.7325°, respectively. At the physical distance of θ¹ Ori C, 373 pc, this corresponds to physical separations of about 3.3 pc and about 24 pc. Regarding the physical distance to our targets, the closest star is ε Per at 82 pc and we measure about solar metallicity for the neutral gas towards this line of sight. Then we measure low metallicity towards the next two closest targets, χ Oph and ρ Oph A at 122 pc and 139 pc, respectively, and with metallicities of 37% and 13% the solar value. Although above we conservatively refer to the distances among the stars themselves, the physical sizes of the pockets of lower-metallicity gas and the distances among them could be smaller. All metallicities are listed in Extended Data Table 3. Thus, we roughly estimate the minimum physical scale of the metallicity variations that we observe to be of the order of tens of parsecs, and possibly down to a few parsecs.

Comparing the metallicity of neutral gas, ionized gas and stars

An interesting open issue is how the neutral gas metallicity is related to the H II regions and in turn to the stellar metallicities. We are not aware of measurements of stellar metallicities of the stars in our sample. For the case of the Orion OB association, ref. [49] found that the B-type stars in the Orion OB association, including in the Orion nebula, have around solar metallicity. The metallicity of the ionized gas in the Orion nebula H II region is debated, ranging from 1/10 solar metallicity (for collisionally excited lines, and in general for refractory elements such as Fe, Mg and Si[50–52] to slightly supersolar[53]. Reference [54] found deviations of up to about 0.4 dex (0.2 dex) from the abundances of nitrogen (oxygen) of ionized gas in H II regions in the Galaxy, after accounting for a radial metallicity gradient. Reference [55] and ref. [10] measured the oxygen metallicity in H II regions in our Galaxy and found metallicity variations over the overall radial gradient of about 0.3 dex over large scales, and smaller along the direction of the long bar. Reference [56] recently found that about 0.5-dex variations of gas-phase metallicity on scales of 100 pc, observed from strong-emission lines diagnostics in Very Large Telescope/Multi Unit Spectroscopic Explorer (MUSE) data of nearby galaxies, positively correlate with the variations in star-formation rates, which they interpret as due to time variations of the star-formation efficiency and including gas infall in their gas-regulated theoretical models. With similar observational techniques, ref. [57] found that the metallicity of H II regions in nearby galaxies show deviations of up to 0.2–0.3 dex from the radial gradients, and that these variations decrease at smaller scales[58].

Comparison with our results is not straightforward. First, H II regions comprise ionized dense gas that is associated with active star formation, while the diffuse neutral gas that we probe here is not necessarily connected to recent star-formation activity. Second, here we probe individual lines of sight, down to very small projected physical scales of a few parsecs. Such small-scale variations can be observationally smoothed away in integrated measurements of metallicity over larger scales, which is normally the case for nearby galaxies. In addition, H II measurements can also be affected by dust depletion, including for the most commonly used reference element, oxygen.

Data availability

The observational data used in this work are publicly available in the Mikulski Archive for Space Telescope (HST/STIS data, programme ID 15335, principal investigator A.D.C., https://doi.org/10.17909/t9-r14v-tp03) and the ESO Science Archive Facility (VLT/UVES data http://archive.eso.org/wdb/wdb/adp/phase3_spectral/form?). The data used in the figures and tables are available as electronically readable source data files, except for the publicly available observational data (Extended Data Fig. 1). Source data are provided with this paper.

Code availability

The VoigtFit software is publicly available on GitHub at https://github.com/jkrogager/VoigtFit.

30. Welty, D. E. & Crowther, P. A. Interstellar Ti II in the Milky Way and Magellanic Clouds. *Mon. Not. R. Astron. Soc.* **404**, 1321–1348 (2010).
31. Diplas, A. & Savage, B. D. An IUE survey of interstellar H I Ly α absorption. I. Column densities. *Astrophys. J. Suppl. Ser.* **93**, 211–228 (1994).
32. Savage, B. D., Bohlin, R. C., Drake, J. F. & Budich, W. A survey of interstellar molecular hydrogen. I. *Astrophys. J.* **216**, 291–307 (1977).
33. Gaia Collaboration et al. The Gaia mission. *Astron. Astrophys.* **595**, A1 (2016).
34. Gaia Collaboration et al. Gaia Data Release 2. Summary of the contents and survey properties. *Astron. Astrophys.* **616**, A1 (2018).
35. Welty, D. E., Sonnentrucker, P., Snow, T. P. & York, D. G. HD 62542: probing the bare, dense core of a translucent interstellar cloud. *Astrophys. J.* **897**, 36, (2020).
36. Valencic, L. A., Clayton, G. C. & Gordon, K. D. Ultraviolet extinction properties in the Milky Way. *Astrophys. J.* **616**, 912–924 (2004).
37. Savage, B. D. & Sembach, K. R. The analysis of apparent optical depth profiles for interstellar absorption lines. *Astrophys. J.* **379**, 245–259 (1991).
38. Jenkins, E. B. A procedure for correcting the apparent optical depths of moderately saturated interstellar absorption lines. *Astrophys. J.* **471**, 292–301 (1996).
39. Sembach, K. R. & Savage, B. D. Observations of highly ionized gas in the Galactic halo. *Astrophys. J. Suppl. Ser.* **83**, 147–201 (1992).
40. Bowen, D. V. et al. The Far Ultraviolet Spectroscopic Explorer Survey of O VI absorption in the disk of the Milky Way. *Astrophys. J. Suppl. Ser.* **176**, 59–163 (2008).
41. Krogager, J.-K. VoigtFit: a Python package for Voigt profile fitting. Preprint at https://arxiv.org/abs/1803.01187 (2018).
42. Price, R. J., Crawford, I. A., Barlow, M. J. & Howarth, I. D. An ultra-high-resolution study of the interstellar medium towards Orion. *Mon. Not. R. Astron. Soc.* **328**, 555–582 (2001).
43. Phillips, A. P., Gondhalekar, P. M. & Pettini, M. A study of element depletions in interstellar gas. *Mon. Not. R. Astron. Soc.* **200**, 687–703 (1982).
44. Jenkins, E. B., Savage, B. D. & Spitzer, L. Jr Abundances of interstellar atoms from ultraviolet absorption lines. *Astrophys. J.* **301**, 355–379 (1986).
45. Roman-Duval, J. et al. METAL: The Metal Evolution, Transport, and Abundance in the Large Magellanic Cloud Hubble program. II. Variations of interstellar depletions and dust-to-gas ratio within the LMC. *Astrophys. J.* **910**, 95 (2021).
46. De Cia, A. Metals and dust in the neutral ISM: the Galaxy, Magellanic Clouds, and damped Lyman-α absorbers *Astron. Astrophys.* **613**, L2 (2018).
47. Jenkins, E. B. A closer look at some gas-phase depletions in the ISM: trends for O, Ge, and Kr versus $F*$, $f(H_2)$, and starlight intensity. *Astrophys. J.* **872**, 55 (2019).
48. De Cia, A., Ledoux, C., Petitjean, P. & Savaglio, S. The cosmic evolution of dust-corrected metallicity in the neutral gas. *Astron. Astrophys.* **611**, A76 (2018).
49. Simón-Díaz, S. The chemical composition of the Orion star forming region. I. Homogeneity of O and Si abundances in B-type stars. *Astron. Astrophys.* **510**, A22 (2010).
50. Rubin, R. H., Dufour, R. J. and Walter, D. K. Silicon and carbon abundances in the Orion nebula. *Astrophys. J.* **413**, 242–250 (1993).
51. Garnett, D. R. et al. Si/O abundance ratios in extragalactic H II regions from Hubble Space Telescope UV spectroscopy. *Astrophys. J.* **449**, L77–L81 (1995).
52. Simón-Díaz, S. & Stasińska, G. The chemical composition of the Orion star forming region. II. Stars, gas, and dust: the abundance discrepancy conundrum. *Astron. Astrophys.* **526**, A48 (2011).
53. Esteban, C. et al. A reappraisal of the chemical composition of the Orion nebula based on Very Large Telescope echelle spectrophotometry. *Mon. Not. R. Astron. Soc.* **355**, 229–247 (2004).
54. Esteban, C. & García-Rojas, J. Revisiting the radial abundance gradients of nitrogen and oxygen of the Milky Way. *Mon. Not. R. Astron. Soc.* **478**, 2315–2336 (2018).
55. Balser, D. S., Wenger, T. V., Anderson, L. D. and Bania, T. M. Azimuthal metallicity structure in the Milky Way Disk. *Astrophys. J.* **806**, 199 (2015).
56. Wang, E. & Lilly, S. J. Gas-phase metallicity as a diagnostic of the drivers of star-formation on different scales. *Astrophys. J.* **910**, 137 (2021).
57. Kreckel, K. et al. Mapping metallicity variations across nearby Galaxy disks. *Astrophys. J.* **887**, 80 (2019).
58. Kreckel, K. et al. Measuring the mixing scale of the ISM within nearby spiral galaxies. *Mon. Not. R. Astron. Soc.* **499**, 193–209 (2020).
59. McMillan, P. J. Mass models of the Milky Way. *Mon. Not. R. Astron. Soc.* **414**, 2446–2457 (2011).
60. Cashman, F. H., Kulkarni, V. P., Kisielius, R., Ferland, G. J. & Bogdanovich, P. Atomic data revisions for transitions relevant to observations of interstellar, circumgalactic, and intergalactic matter. *Astrophys. J. Suppl. Ser.* **230**, 8 (2017).
61. Morton, D. C. Atomic data for resonance absorption lines. III. Wavelengths longward of the Lyman limit for the elements hydrogen to gallium. *Astrophys. J. Suppl. Ser.* **149**, 205–238 (2003).
62. Boissé, P. & Bergeron, J. Improved Ni II oscillator strengths from quasar absorption systems. *Astron. Astrophys.* **622**, A140 (2019).
63. Kisielius, R. et al. Atomic data for Zn II: improving spectral diagnostics of chemical evolution in high-redshift galaxies. *Astrophys. J.* **804**, 76 (2015).
64. Jenkins, E. B. & Tripp, T. M. Measurements of the *f*-values of the resonance transitions of Ni II at 1317.217 and 1370.132 Å. *Astrophys. J.* **637**, 548–552 (2006).
65. Wiseman, P. et al. Evolution of the dust-to-metals ratio in high-redshift galaxies probed by GRB-DLAs. *Astron. Astrophys.* **599**, A24 (2017).

Author contributions A.D.C. initiated, designed and directed the project, is the principal investigator of the HST data, analysed and interpreted the data, developed and applied the main methodology, and wrote the bulk of the manuscript. E.B.J. reduced the HST data and retrieved the UVES data, analysed and interpreted the data, measured the column densities, developed and applied one of the two methods to measure the metallicity, contributed to the writing and produced Fig. 3. A.J.F. contributed to the writing and scientific design of the paper. C.L. checked the consistency of the analysis, helped interpret the data and contributed to the writing. E.B.J., C.L., A.J.F. and P.P. are co-investigators of the HST data. T.R.-H. measured the position of our targets within the Galaxy and produced Fig. 1 and Extended Data Fig. 4. C.K. reviewed the depletion methods and assumptions, and collected data from Galactic extinction maps. P.P. contributed to the prioritization of the scientific goals and the writing. J.-K.K. assessed the ionization effects and contributed to the writing. J.-K.K., T.R.-H., C.K., C.L. and A.D.C. measured the column densities towards eight targets with an independent method for a cross-check of the results. All authors participated in the scientific interpretation, edited the manuscript and contributed to its revision.
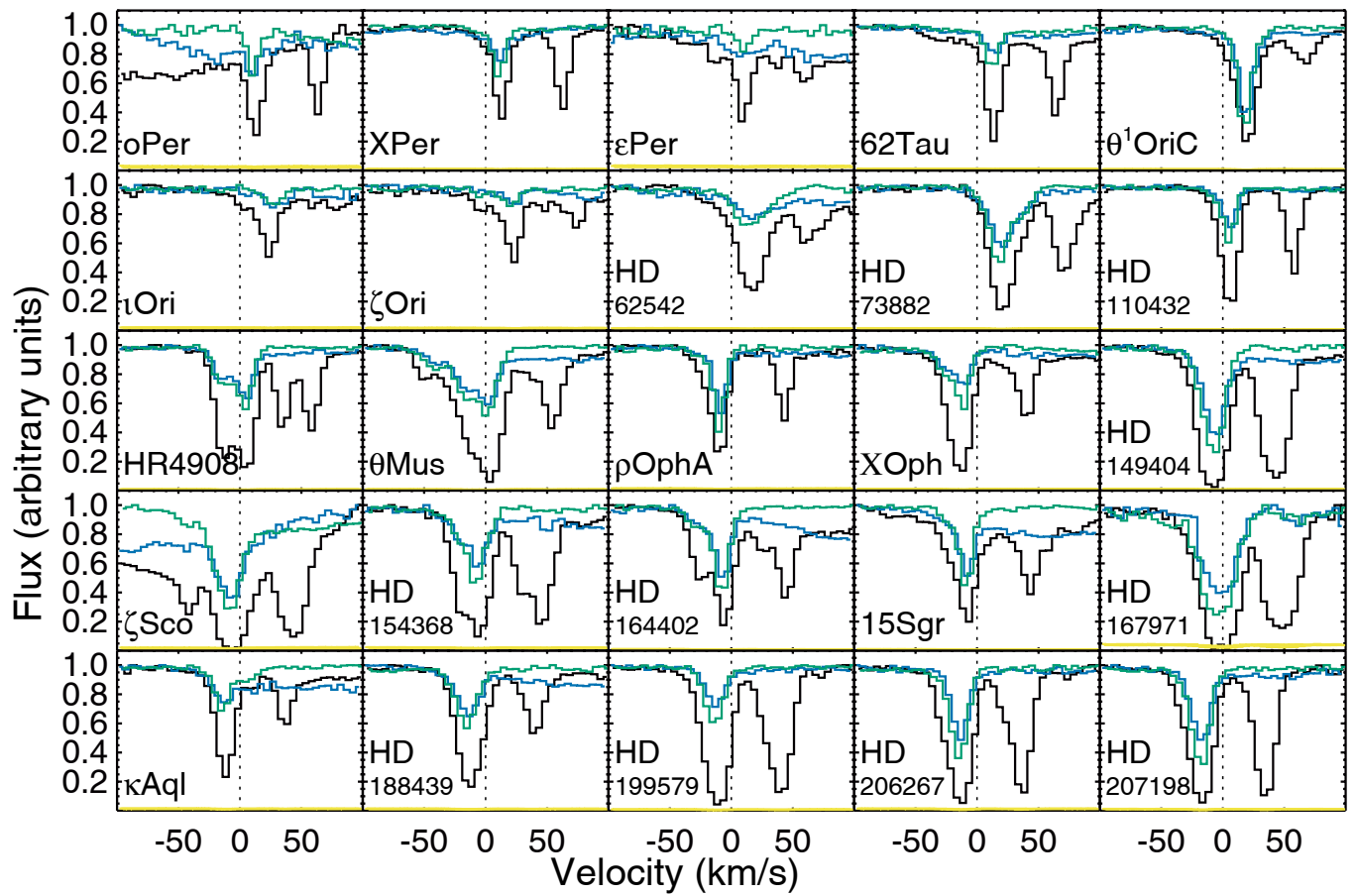
Extended Data Fig. 1 | Line profiles of Zn II λ2026 (black), Cr II λ2056 (blue) and Fe II λ2260 (green) in our sample. The Mg I λ2026 line is separated by -50 km s^{-1} from Zn II. Vertical lines mark the zero-velocity central wavelength of the Zn II line. The yellow curve shows the 1σ uncertainties.
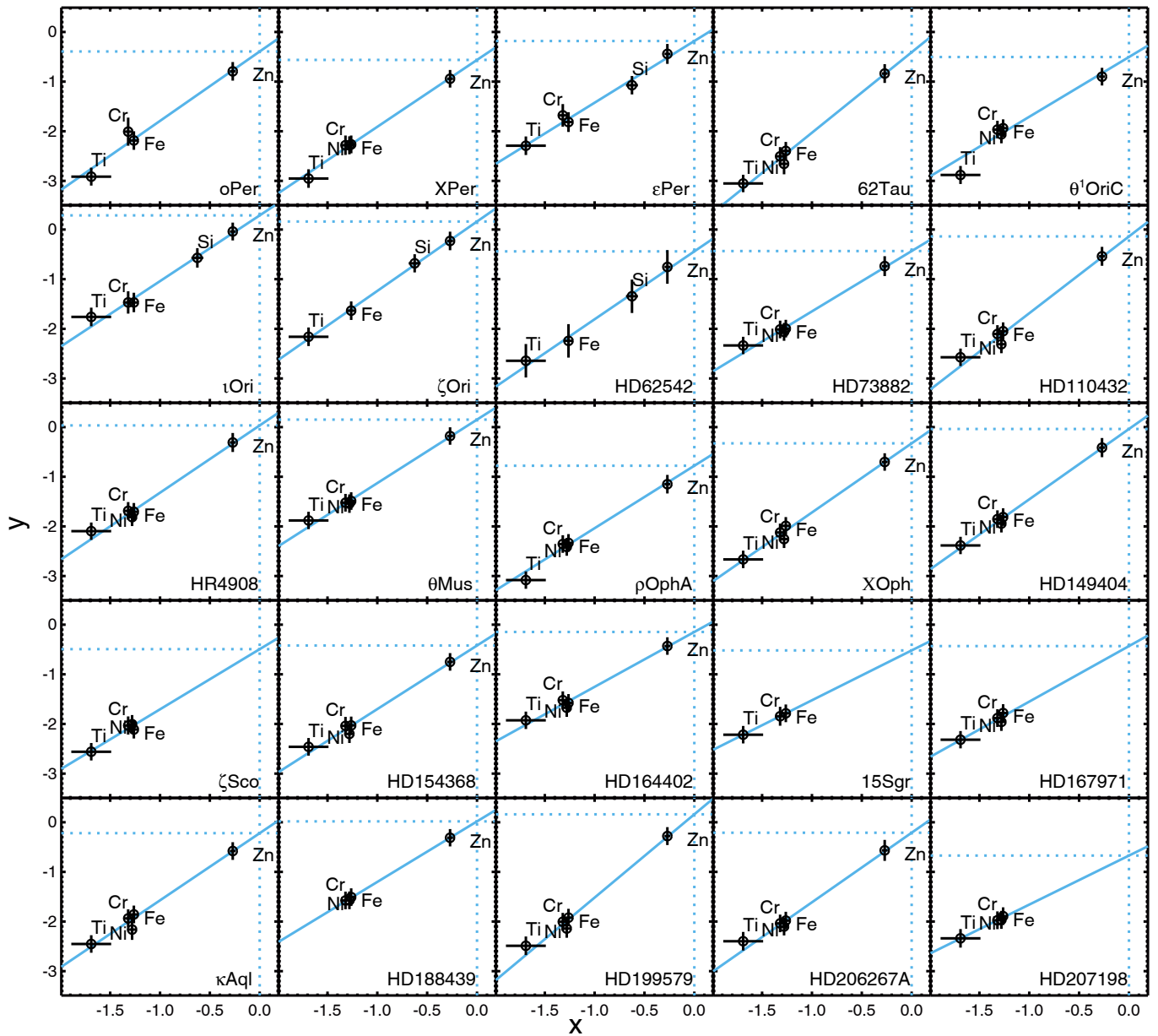
Extended Data Fig. 2 | Determination of the metallicity and strength of depletion with the relative method. The variables and coefficients of the linear relation are defined in equations (4) to (7), where the y intercept gives the $[M/H]_{tot}$ and the slope of the relation the strength of depletion $[Zn/Fe]_{fit}$. The error bars show the 1σ uncertainties.
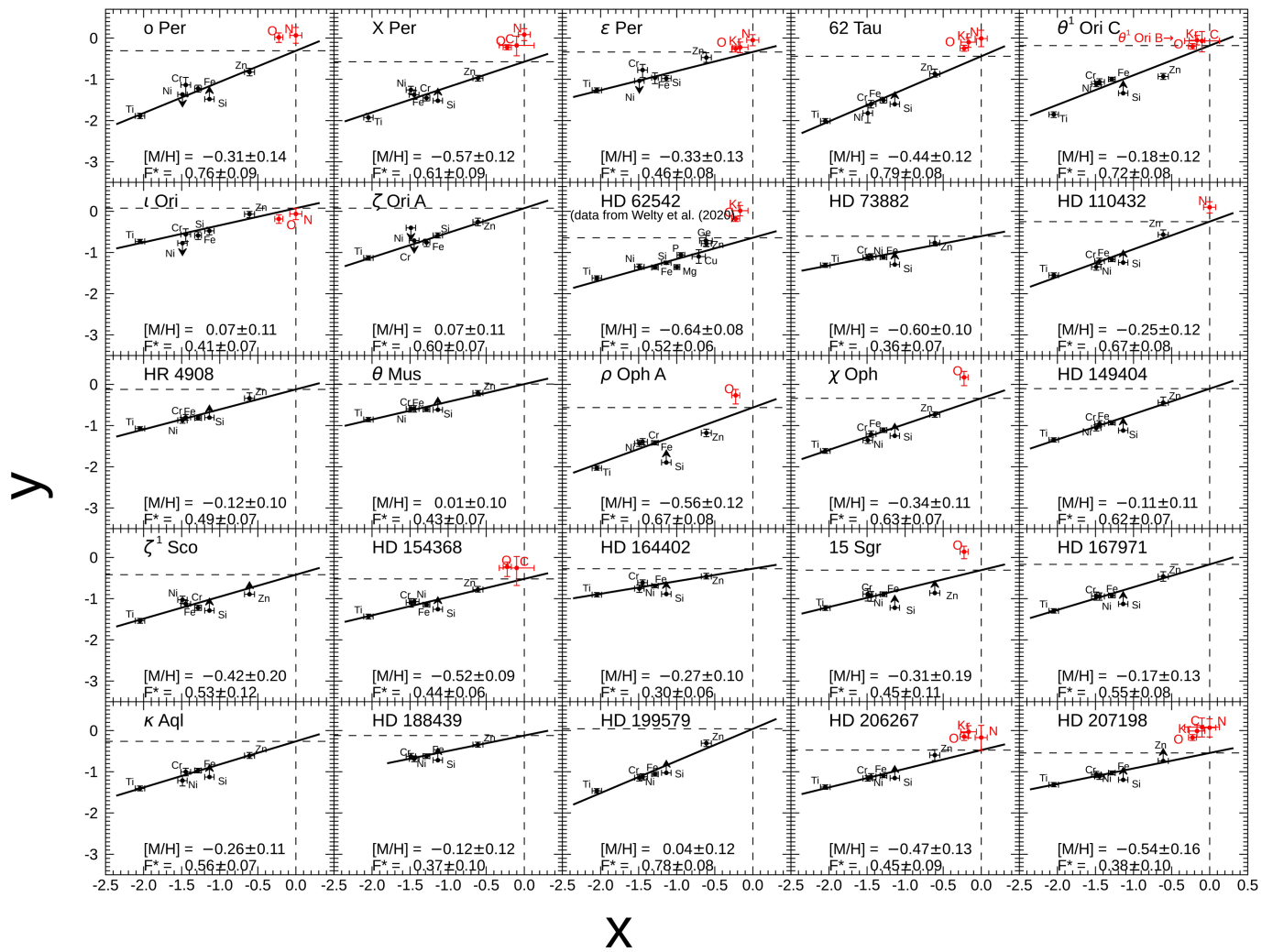
Extended Data Fig. 3 | Determination of [M/H]$_{tot}$ and F^* with the F^* method. The variables are described in equation (8). The most volatile elements (red) are taken from the literature (Extended Data Table 6) and shown for reference: their discrepancy with respect to the more refractory elements suggests a mix between high-metallicity and pristine gas, see Methods. The error bars show the 1σ uncertainties.
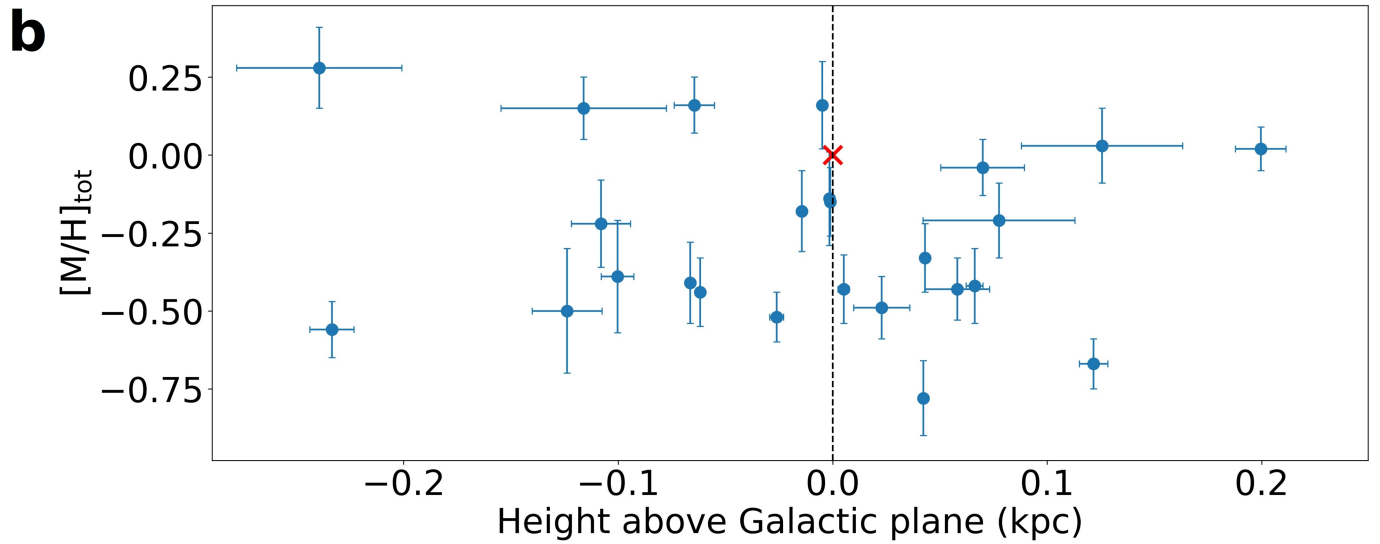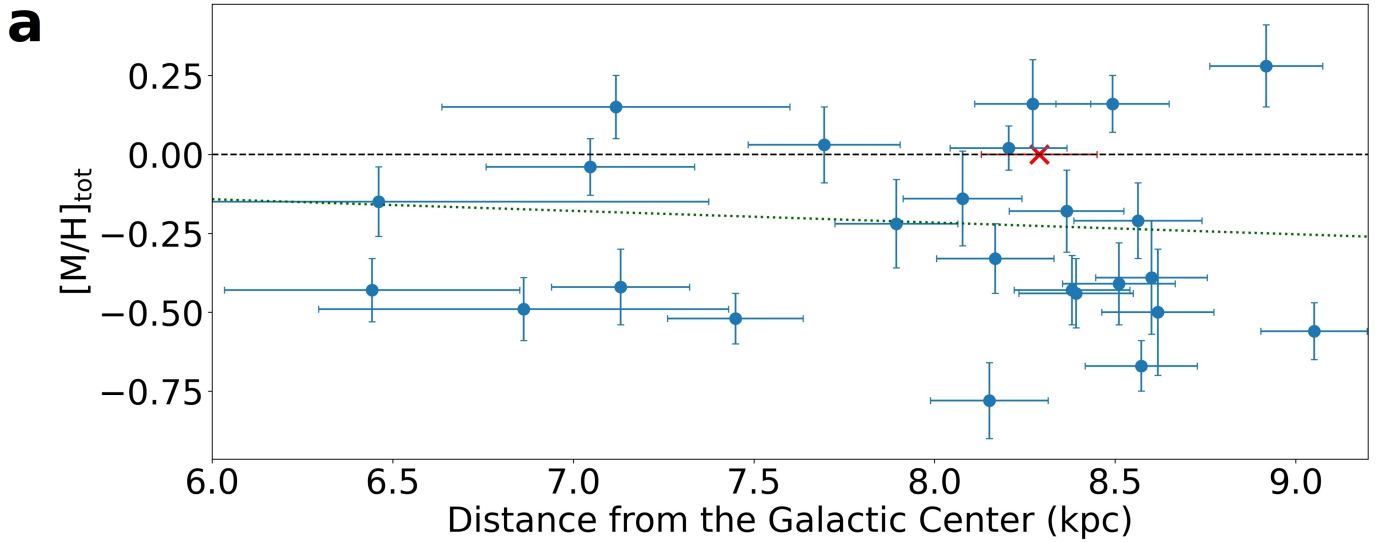
Extended Data Fig. 4 | Metallicity towards our targets and their Galactic location. a, Metallicities towards our targets and their Galactic radii. The green dotted line shows the metallicity gradient measured in H II regions by ref. [10], although without dust corrections. The solar Galactic radius (red cross) is assumed at 8.29 kpc [59]. The error bars show the 1σ uncertainties. **b**, Metallicities towards our targets and their height above the Galactic Disk. The error bars show the 1σ uncertainties.

Article

Extended Data Table 1 | Target sample characteristics

ID	HD	Type	l [deg]	b [deg]	r_{GaiaDR2} [pc]	V [mag]	E(B − V) [mag]	R_V	$\log N(H\,\textsc{i})$	$\log N(H_2)$
o Per	23180	B1IIIB	160.364	−17.740	329 ± 25	3.83	0.31 ± 0.03	3.11 ± 0.39	20.82 ± 0.10	20.60 ± 0.10
X Per	24534	O9.5pe	163.081	−17.136	792 ± 35	6.10	0.59 ± 0.03	−	20.73 ± 0.10	20.92 ± 0.10
ϵ Per	24760	B0.5V+A2	157.354	−10.088	82 ± 6	2.89	0.10 ± 0.03	−	20.45 ± 0.10	19.52 ± 0.10
62 Tau	27778	B3V	172.763	−17.393	222 ± 2	6.36	0.37 ± 0.03	2.59 ± 0.24	20.95 ± 0.10	20.79 ± 0.10
θ^1 Ori C	37022	O6-7p	209.011	−19.384	373 ± 49	5.13	0.34 ± 0.03	5.73 ± 0.69	21.54 ± 0.10	17.25 ± 0.10
ι Ori	37043	O9III	209.522	−19.583	(714 ± 115ᵃ)	2.77	0.07 ± 0.03	−	20.20 ± 0.10	14.69 ± 0.10
ζ Ori A	37742	O9.5Ibe	206.452	−16.585	(226 ± 33ᵃ)	2.05	0.06 ± 0.03	−	20.39 ± 0.10	15.86 ± 0.10
HD 62542	62542	B5V/B3V	255.915	−9.237	385 ± 4	8.04	0.35 ± 0.03	2.82 ± 0.24	20.70 ± 0.18	20.81 ± 0.20
HD 73882	73882	O8V	260.182	0.643	(460 ± 234ᵃ)	7.22	0.70 ± 0.03	3.56 ± 0.13	21.11 ± 0.10	21.11 ± 0.10
HD 110432	110432	B0.5IVpe	301.958	−0.203	416 ± 21	5.31	(0.51 ± 0.03)	−	20.85 ± 0.10	20.64 ± 0.10
HR 4908	112244	O9Ibe	303.553	6.031	(1195 ± 358)	5.32	0.30 ± 0.03	−	21.08 ± 0.10	20.14 ± 0.10
θ Mus	113904	WC6+O6-7V	304.675	−2.491	(2671 ± 887)	5.51	0.25 ± 0.03	−	21.15 ± 0.10	19.83 ± 0.10
ρ Oph A	147933	B2IV	353.686	17.687	139 ± 3	5.02	0.48 ± 0.03	5.74 ± 0.40	21.63 ± 0.10	20.57 ± 0.10
χ Oph	148184	B2IVpe	357.933	20.677	122 ± 4	4.42	(0.52 ± 0.03)	−	21.13 ± 0.10	20.63 ± 0.10
HD 149404	149404	O9Iae	340.538	3.006	(1333 ± 373)	5.47	0.68 ± 0.03	3.53 ± 0.38	21.40 ± 0.10	20.79 ± 0.10
ζ^1 Sco	152236	B1Ia+pe	343.028	0.870	(1507 ± 863)	4.73	(0.68 ± 0.03)	3.73 ± 0.39	21.77 ± 0.10	20.73 ± 0.10
HD 154368	154368	O9Ia	349.970	3.215	1180 ± 70	6.13	0.78 ± 0.03	3.33 ± 0.15	21.00 ± 0.10	21.16 ± 0.10
HD 164402	164402	B0lab/b	7.162	−0.034	(1847 ± 1275)	5.77	0.28 ± 0.03	3.03 ± 0.62	21.11 ± 0.10	19.49 ± 0.10
15 Sgr	167264	O9.7Iab	10.456	−1.741	857 ± 106	5.37	0.34 ± 0.03	3.26 ± 0.31	21.15 ± 0.10	20.28 ± 0.10
HD 167971	167971	O8Iaf(n)+O4/5C	18.251	1.684	(1976 ± 515)	7.45	1.08 ± 0.03	3.44 ± 0.10	21.60 ± 0.10	20.85 ± 0.10
κ Aql	184915	B0.5IIIn	31.771	−13.287	470 ± 60	4.96	0.26 ± 0.03	−	20.90 ± 0.10	20.31 ± 0.10
HD 188439	188439	B0.5IIInC	81.772	10.320	1114 ± 66	6.28	0.14 ± 0.03	−	20.78 ± 0.10	19.95 ± 0.10
HD 199579	199579	O6Ve	85.697	−0.300	918 ± 50	5.96	0.37 ± 0.03	3.17 ± 0.69	21.04 ± 0.10	20.53 ± 0.10
HD 206267	206267	O6.0V((f))+O9:V	99.290	3.738	(1190 ± 543)	5.62	0.53 ± 0.03	2.82 ± 0.16	21.30 ± 0.10	20.86 ± 0.10
HD 207198	207198	O9IIe	103.136	6.995	999 ± 54	5.95	0.62 ± 0.03	2.77 ± 0.35	21.34 ± 0.10	20.83 ± 0.10

In parenthesis are reported unreliable values of E(B − V), because of contamination by strong H-alpha emission, and unreliable values of the Gaia DR2 distance, because of a large parallax uncertainty (that is, parallax-to-error ≤5). ᵃHipparcos distance. H I and H_2 values are taken from ref. [30], with the exception of HD 62542 (from ref. [35]). E(B − V) values are taken from ref. [31] and R_V from ref. [36].

Extended Data Table 2 | Column densities

ID	Mg I	Al II	Si II	Ti II	Cr II	Fe II	Co II	Ni II	Zn II
					log N				
o Per	13.67 ± 0.13	> 12.81	> 15.00	11.16 ± 0.05	12.93 ± 0.22	14.45 ± 0.06	< 13.05	< 13.14	13.00 ± 0.07
X Per	13.68 ± 0.05	> 13.09	> 15.14	11.30 ± 0.07^a	12.84 ± 0.09	14.55 ± 0.03	< 12.13	13.36 ± 0.05	13.03 ± 0.04
ϵ Per	$--$	> 12.69	14.88 ± 0.06	11.16 ± 0.07^a	12.64 ± 0.14	14.20 ± 0.09	< 12.89	< 12.85	12.73 ± 0.10
62 Tau	13.40 ± 0.06	> 12.57	> 15.04	11.18 ± 0.03	12.60 ± 0.06	14.40 ± 0.04	< 12.65	12.97 ± 0.11	13.12 ± 0.08
θ^1 Ori C	13.86 ± 0.08	> 13.24	> 15.52	11.57 ± 0.05	13.35 ± 0.02	15.07 ± 0.02	< 12.59	13.77 ± 0.04	13.27 ± 0.04
ι Ori	$--$	> 13.09	15.04 ± 0.09	11.35 ± 0.07^a	12.51 ± 0.14	14.20 ± 0.09	< 12.71	< 12.77	12.79 ± 0.04
ζ Ori A	< 13.44	> 13.10	15.12 ± 0.05	11.14 ± 0.07^a	< 12.55	14.22 ± 0.06	$--$	< 13.34	12.79 ± 0.07
HD 62542	13.81 ± 0.04	$--$	15.32 ± 0.02	11.52 ± 0.03^a	$--$	14.48 ± 0.02	< 12.60	13.26 ± 0.04	13.13 ± 0.05
HD 73882	13.41 ± 0.14	> 13.39	> 15.61	12.16 ± 0.02	13.35 ± 0.02	15.06 ± 0.02	12.83 ± 0.22	13.82 ± 0.04	13.48 ± 0.10
HD 110432	13.62 ± 0.03	> 12.97	> 15.27	11.53 ± 0.03	12.87 ± 0.03	14.62 ± 0.03	< 12.25	13.19 ± 0.04	13.29 ± 0.08
HR 4908	13.73 ± 0.06	> 13.30	> 15.68	11.98 ± 0.02	13.26 ± 0.02	14.93 ± 0.02	< 12.40	13.65 ± 0.04	13.49 ± 0.08
θ Mus	13.39 ± 0.14	> 13.58	> 15.89	12.22 ± 0.02	13.44 ± 0.03	15.17 ± 0.02	13.12 ± 0.13	13.94 ± 0.06	13.64 ± 0.03
ρ Oph A	13.54 ± 0.04	> 12.98	> 15.12	11.53 ± 0.02	13.12 ± 0.02	14.84 ± 0.02	< 12.60	13.58 ± 0.03	13.18 ± 0.07
χ Oph	13.49 ± 0.06	> 13.05	> 15.41	11.59 ± 0.03	12.99 ± 0.03	14.82 ± 0.02	< 12.73	13.38 ± 0.04	13.27 ± 0.03
HD 149404	14.16 ± 0.03	> 13.40	> 15.77	12.10 ± 0.02	13.49 ± 0.02	15.23 ± 0.02	13.14 ± 0.14	13.93 ± 0.03	13.79 ± 0.09
ζ^1 Sco	> 14.29	> 13.58	> 15.87	12.19 ± 0.03	13.59 ± 0.05	15.20 ± 0.05	$--$	14.13 ± 0.06	> 13.61
HD 154368	14.04 ± 0.09	> 13.28	> 15.65	12.04 ± 0.04	13.32 ± 0.05	15.03 ± 0.03	< 12.67	13.69 ± 0.05	13.47 ± 0.04
HD 164402	13.40 ± 0.18	> 13.38	> 15.56	12.11 ± 0.02	13.38 ± 0.02	15.02 ± 0.02	< 13.10	13.75 ± 0.05	13.33 ± 0.04
15 Sgr	13.42 ± 0.14	> 13.49	> 15.35	11.95 ± 0.03	13.18 ± 0.08	14.94 ± 0.03	$--$	13.72 ± 0.14	> 13.05
HD 167971	14.25 ± 0.05	> 13.45	> 15.92	12.32 ± 0.02	13.62 ± 0.03	15.42 ± 0.03	< 13.35	14.07 ± 0.04	> 13.70
κ Aql	13.32 ± 0.13	> 13.23	> 15.27	11.54 ± 0.03	12.92 ± 0.05	14.69 ± 0.03	13.01 ± 0.23	13.22 ± 0.11	13.13 ± 0.04
HD 188439	13.28 ± 0.09	> 13.22	> 15.49	$--$	13.09 ± 0.03	14.85 ± 0.02	< 12.54	13.62 ± 0.03	13.21 ± 0.02
HD 199579	13.93 ± 0.06	> 13.18	> 15.54	11.67 ± 0.07^a	13.02 ± 0.04	14.80 ± 0.02	< 12.24	13.40 ± 0.06	13.60 ± 0.05
HD 206267	14.06 ± 0.03	> 13.23	> 15.70	12.05 ± 0.07^a	13.27 ± 0.02	15.02 ± 0.02	< 12.73	13.73 ± 0.03	13.60 ± 0.12
HD 207198	14.21 ± 0.06	> 13.36	> 15.67	12.12 ± 0.07^a	13.35 ± 0.03	15.13 ± 0.02	13.19 ± 0.13	13.88 ± 0.05	> 13.47

They are measured from the HST/STIS data of the 25 stars in our sample. [a]Measurements from ref. [30].

Article

Extended Data Table 3 | Metallicities of the neutral ISM

ID	$\log N(H)$	[Zn/H]	[Zn/Fe]	$[Zn/Fe]_{fit}$	$[M/H]_{tot,[X/Y]}$	$F*$	$[M/H]_{tot,F*}$	Z-test
o Per	21.16 ± 0.17	-0.79 ± 0.16	1.40 ± 0.09	1.40 ± 0.11	-0.39 ± 0.18	0.76 ± 0.09	-0.31 ± 0.14	-0.36
X Per	21.34 ± 0.17	-0.94 ± 0.15	1.33 ± 0.05	1.35 ± 0.07	-0.56 ± 0.09	0.61 ± 0.09	-0.57 ± 0.12	0.05
ϵ Per	20.54 ± 0.17	-0.44 ± 0.17	1.38 ± 0.14	1.24 ± 0.13	-0.18 ± 0.13	0.46 ± 0.08	-0.33 ± 0.13	0.81
62 Tau	21.33 ± 0.17	-0.84 ± 0.16	1.56 ± 0.09	1.62 ± 0.10	-0.41 ± 0.13	0.79 ± 0.08	-0.44 ± 0.12	0.18
θ^1 Ori C	21.54 ± 0.17	-0.90 ± 0.15	1.04 ± 0.05	1.20 ± 0.06	-0.50 ± 0.20	0.72 ± 0.08	-0.18 ± 0.12	-1.41
ι Ori	20.20 ± 0.17	-0.04 ± 0.15	1.43 ± 0.10	1.32 ± 0.10	0.28 ± 0.13	0.41 ± 0.07	0.07 ± 0.11	1.27
ζ Ori A	20.39 ± 0.17	-0.23 ± 0.16	1.41 ± 0.10	1.40 ± 0.11	0.16 ± 0.09	0.61 ± 0.07	0.11 ± 0.11	0.37
HD 62542	21.25 ± 0.34	-0.75 ± 0.15	1.50 ± 0.05	1.37 ± 0.09	-0.44 ± 0.11	0.48 ± 0.06	-0.69 ± 0.07	1.90
HD 73882	21.59 ± 0.17	-0.74 ± 0.17	1.26 ± 0.10	1.21 ± 0.11	-0.43 ± 0.11	0.36 ± 0.07	-0.60 ± 0.10	1.14
HD 110432	21.20 ± 0.17	-0.54 ± 0.16	1.51 ± 0.08	1.55 ± 0.10	-0.14 ± 0.15	0.67 ± 0.08	-0.25 ± 0.08	0.65
HR 4908	21.17 ± 0.17	-0.31 ± 0.16	1.40 ± 0.08	1.36 ± 0.10	0.03 ± 0.12	0.49 ± 0.07	-0.12 ± 0.10	0.98
θ Mus	21.19 ± 0.17	-0.18 ± 0.14	1.32 ± 0.04	1.28 ± 0.06	0.15 ± 0.10	0.43 ± 0.07	0.01 ± 0.10	1.01
ρ Oph A	21.70 ± 0.17	-1.15 ± 0.16	1.19 ± 0.07	1.26 ± 0.08	-0.78 ± 0.12	0.67 ± 0.08	-0.56 ± 0.12	-1.30
χ Oph	21.34 ± 0.17	-0.70 ± 0.14	1.29 ± 0.04	1.39 ± 0.07	-0.33 ± 0.11	0.63 ± 0.07	-0.34 ± 0.11	0.08
HD 149404	21.57 ± 0.17	-0.41 ± 0.17	1.41 ± 0.09	1.42 ± 0.10	-0.04 ± 0.09	0.62 ± 0.07	-0.11 ± 0.11	0.51
ζ^1 Sco	21.84 ± 0.17	> -0.86	> 1.26	1.21 ± 0.88	-0.49 ± 0.10	0.53 ± 0.12	-0.42 ± 0.20	-0.33
HD 154368	21.59 ± 0.17	-0.75 ± 0.15	1.29 ± 0.04	1.28 ± 0.07	-0.42 ± 0.12	0.44 ± 0.06	-0.52 ± 0.09	0.67
HD 164402	21.13 ± 0.17	-0.43 ± 0.15	1.15 ± 0.04	1.11 ± 0.06	-0.15 ± 0.11	0.30 ± 0.06	-0.27 ± 0.10	0.85
15 Sgr	21.25 ± 0.17	> -0.83	> 0.96	1.00 ± 0.51	-0.52 ± 0.08	0.45 ± 0.11	-0.31 ± 0.19	-1.01
HD 167971	21.73 ± 0.17	> -0.66	> 1.12	1.12 ± 1.37	-0.43 ± 0.10	0.55 ± 0.08	-0.17 ± 0.13	-1.60
κ Aql	21.08 ± 0.17	-0.58 ± 0.15	1.28 ± 0.05	1.35 ± 0.07	-0.22 ± 0.14	0.56 ± 0.07	-0.26 ± 0.11	0.23
HD 188439	20.89 ± 0.17	-0.31 ± 0.14	1.20 ± 0.03	1.22 ± 0.06	0.02 ± 0.07	0.37 ± 0.10	-0.12 ± 0.12	0.97
HD 199579	21.25 ± 0.17	-0.28 ± 0.15	1.65 ± 0.06	1.68 ± 0.08	0.16 ± 0.14	0.78 ± 0.08	0.04 ± 0.12	0.65
HD 206267	21.54 ± 0.17	-0.57 ± 0.19	1.42 ± 0.12	1.40 ± 0.13	-0.21 ± 0.12	0.45 ± 0.09	-0.47 ± 0.13	1.45
HD 207198	21.55 ± 0.17	> -0.71	> 1.19	0.99 ± 0.58	-0.67 ± 0.08	0.38 ± 0.10	-0.54 ± 0.16	-0.74

These are derived using dust corrections from the relative method ($[M/H]_{tot,[X/Y]}$) and the $F*$ method $[M/H]_{tot,F*}$. The last column reports the difference between the two in σ levels from a Z-test.

Extended Data Table 4 | Absorption lines that we use in this work and their oscillator strengths

Ion	λ [Å]	$\log \lambda f$	Ref.
Mg I	1827.935	1.677	[60]
Mg I	2026.477	2.36	[60]
Al II	1670.787	3.463	[60]
Si II	1808.013	0.646	[60]
Ti II	3384.740	3.127	[60]
Ti II	3242.929	2.919	[60]
Ti II	3230.131	2.377	[60]
Cr II	2056.254	2.351	[60]
Cr II	2062.234	2.224	[60]
Cr II	2066.161	2.015	[60]
Fe II	2344.214	2.427	[60,61]
Fe II	2260.780	0.742	[60,61]
Fe II	2249.877	0.612	[60,61]
Co II	2012.161	1.87	[60]
Co II	1941.280	1.82	[60]
Ni II	1741.549	1.876	[62]
Ni II	1709.600	1.735	[62]
Ni II	1751.910	1.691	[62]
Zn II	2026.136	3.106	[63]
Zn II	2062.664	2.804	[63]

We use f-values from refs. [60,61,62,63]. For Ni transitions, we used the *f*-values from ref. [62] based on observational data, which agree with ref. [64], instead of the theoretical measurements of ref. [60].

Article

Extended Data Table 5 | Coefficients used in equations (6) and (7)

X	$A2_X$	$B2_X$
Mg	-0.07 ± 0.05	-0.61 ± 0.05
Al	-0.27 ± 0.00	0.00 ± 0.00
Si	-0.10 ± 0.03	-0.63 ± 0.06
Cr	0.13 ± 0.03	-1.32 ± 0.04
Fe	-0.01 ± 0.03	-1.26 ± 0.04
Ni	0.09 ± 0.03	-1.28 ± 0.04
Zn	0.00 ± 0.01	-0.27 ± 0.03
Ti	-0.04 ± 0.01	-1.69 ± 0.20

They are taken from the literature, from ref. [9] except for Ni and Ti (from ref. [65]), but here updated for the most recent f-values, listed in Extended Data Table 4.

Extended Data Table 6 | Column densities of the volatile elements

ID	$O\,I_{MIN}$	$O\,I$	$O\,I_{MAX}$	$Kr\,I_{MIN}$	$Kr\,I$	$Kr\,I_{MAX}$	$C\,II_{MIN}$	$C\,II$	$C\,II_{MAX}$	$N\,II_{MIN}$	$N\,II$	$N\,II_{MAX}$
o Per	17.82	17.93	18.02	–	–	–	–	–	–	16.87	17.02	17.17
X Per	17.85	17.87	17.89	–	–	–	17.35	17.51	17.62	17.14	17.22	17.30
ϵ Per	16.98	17.03	17.07	11.38	11.46	11.53	–	–	–	16.22	16.28	16.35
62 Tau	17.79	17.83	17.87	12.31	12.37	12.41	–	–	–	16.95	17.11	17.27
θ^1 Ori C	18.06	18.09	18.12	12.59	12.63	12.67	17.64	17.82	17.94	–	–	–
ι Ori	16.67	16.76	16.84	–	–	–	–	–	–	15.86	15.93	15.99
HD 62542	17.80	17.82	17.80	12.30	12.41	12.52	–	–	–	–	–	–
HD 110432	–	–	–	–	–	–	–	–	–	17.02	17.09	17.15
ρ Oph A	17.98	18.18	18.31	–	–	–	–	–	–	–	–	–
χ Oph	18.07	18.26	18.39	–	–	–	–	–	–	–	–	–
HD 154368	17.88	18.11	18.21	–	–	–	17.30	17.68	17.88	–	–	–
15 Sgr	17.98	18.14	18.26	–	–	–	–	–	–	–	–	–
HD 206267	18.07	18.10	18.13	12.49	12.59	12.67	–	–	–	16.87	17.16	17.43
HD 207198	18.12	18.15	18.18	12.58	12.67	12.74	17.84	17.98	18.09	17.22	17.41	17.59

These values are taken from refs. [8,47].